

See discussions, stats, and author profiles for this publication at: <https://www.researchgate.net/publication/263354587>

# Real-Time Ab Initio KMC Simulation of the Self-Assembly and Sintering of Bimetallic Epitaxial Nanoclusters: Au + Ag on Ag(100)

ARTICLE in NANO LETTERS · JUNE 2014

Impact Factor: 13.59 · DOI: 10.1021/nl5017128 · Source: PubMed

---

CITATIONS

5

READS

62

## 3 AUTHORS:



[Yong Han](#)

Iowa State University

62 PUBLICATIONS 464 CITATIONS

[SEE PROFILE](#)



[Da-Jiang Liu](#)

106 PUBLICATIONS 1,384 CITATIONS

[SEE PROFILE](#)



[James Evans](#)

Iowa State University

260 PUBLICATIONS 6,447 CITATIONS

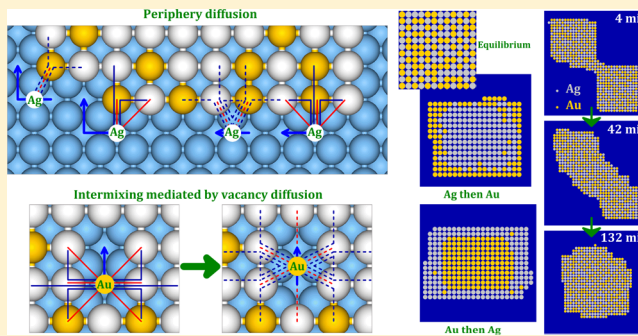
[SEE PROFILE](#)

# Real-Time Ab Initio KMC Simulation of the Self-Assembly and Sintering of Bimetallic Epitaxial Nanoclusters: Au + Ag on Ag(100)

Yong Han,<sup>†,\*</sup> Da-Jiang Liu,<sup>‡</sup> and James W. Evans<sup>†,‡</sup>

<sup>†</sup>Department of Physics and Astronomy and <sup>‡</sup>Division of Chemical and Biological Sciences, Ames Laboratory – USDOE, Iowa State University, Ames, Iowa 50011, United States

**ABSTRACT:** Far-from-equilibrium shape and structure evolution during formation and post-assembly sintering of bimetallic nanoclusters is extremely sensitive to the periphery diffusion and intermixing kinetics. Precise characterization of the many distinct local-environment-dependent diffusion barriers is achieved for epitaxial nanoclusters using density functional theory to assess interaction energies both with atoms at adsorption sites and at transition states. Kinetic Monte Carlo simulation incorporating these barriers then captures structure evolution on the appropriate time scale for two-dimensional core-ring and intermixed Au–Ag nanoclusters on Ag(100).



**KEYWORDS:** Bimetallic nanoclusters, intermixing, self-assembly, sintering, stochastic modeling, KMC simulation, DFT energetics

**M**ajor advances have been achieved in the control of shapes, structures, and composition profiles of bimetallic nanoclusters (NCs), an effort motivated in part by applications to catalysis and plasmonics. Self-assembly of such three-dimensional (3D) NCs can be achieved via liquid-phase synthesis<sup>1–3</sup> and of either 2D<sup>4–6</sup> or 3D<sup>7,8</sup> NCs by deposition onto smooth surfaces. In either case, these processes generally occur far from equilibrium, and the resultant structures are usually highly sensitive to the thermally activated kinetics of relaxation (via periphery diffusion, attachment-detachment, and/or intermixing) for the aggregated atoms.<sup>9–11</sup> Thus, a major complication and obstacle for complete characterization and modeling of self-assembly is that these relaxation rates and associated barriers depend strongly on the vast number of possible local environments (including distinct periphery shapes and compositional configurations) of the diffusive relaxation processes. Also, realistic modeling must track the delicate competition between NC growth and relaxation, which controls structure, on the appropriate time scale.

An extensive heuristic understanding of the diverse variety of 3D NC growth shapes from cubes, cuboctahedra, and so forth, to platelets to rods has been developed based on relative facet growth rates<sup>1,2</sup> and simplified coarse-grained modeling.<sup>12</sup> The role of periphery diffusion was recently emphasized.<sup>3</sup> However, analysis of single-component 2D epitaxial systems has shown that not just the extent of periphery diffusion along faceted sides or edges, but the fine details of inhibition and anisotropy in corner-rounding are critical.<sup>10,11</sup> Also, dynamics of shape evolution on nanoscale can differ fundamentally from coarse-grained continuum descriptions.<sup>13</sup> Additional insight into NC structure, that is, single- and multicore–shell versus mixed versus porous or hollow, and so forth, has often exploited classic macroscale materials science concepts regarding

vacancy-mediated intermixing kinetics and related Kirkendall voiding.<sup>14,15</sup> However, what has been lacking is an effective approach for precise ab initio atomistic-level quantification of these phenomena.

Low-strain 2D epitaxial NCs formed by deposition on crystalline surfaces constitute a class of systems offering significant advantages for realistic modeling.<sup>10,11</sup> Adsorbed atoms (adatoms) are localized to a periodic array of adsorption sites. Modeling of NC self-assembly then requires description of random deposition onto these sites and of subsequent diffusive hopping of adatoms between nearest-neighbor (NN) sites (assuming that this is the dominant surface diffusion mechanism). Surface diffusion processes include both terrace diffusion mediated aggregation into 2D NCs, and relaxation within those NCs. Diffusive hop rates have an Arrhenius form  $h_\alpha = \nu e^{-E_{\text{act}}(\alpha)/(k_b T)}$  for each adspecies  $\alpha$ , where  $T$  denotes the surface temperature and  $\nu$  is an attempt frequency. The critical challenge is a precise specification of the local-environment-dependent activation barriers  $E_{\text{act}}(\alpha)$ . These must also be consistent with the system thermodynamics that is prescribed by specifying interactions between adatoms on nearby adsorption sites. The overall process is described by a stochastic lattice-gas (LG) model that can be analyzed by kinetic Monte Carlo (KMC) simulation on the appropriate time scale of tens of seconds for NC formation and usually tens of minutes for post-assembly NC sintering.

Below,  $E_d(\alpha)$  denotes the terrace diffusion barrier for an isolated adspecies  $\alpha$ , and  $\Phi(\text{init})$ ,  $\Phi(\text{TS})$ , and  $\Phi(\text{fnl})$  denote

**Received:** May 7, 2014

**Revised:** June 12, 2014

**Published:** June 24, 2014



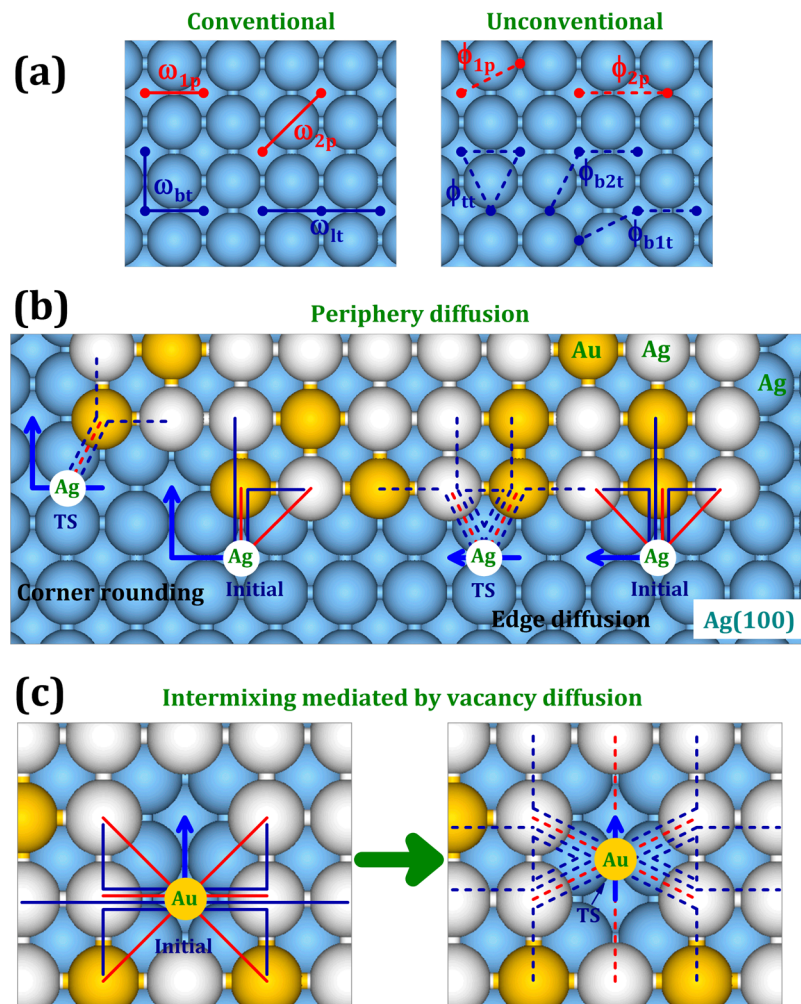


**Figure 1.** (a) Conventional pair interactions:  $\omega_{1p}$  (separation  $d = a$ ) and  $\omega_{2p}$  ( $d = \sqrt{2}a$ ) where  $a = 0.289$  nm is the surface lattice constant. Trio interactions:  $\omega_{lt}$  (linear) and  $\omega_{bt}$  (bent). Unconventional pair interactions:  $\phi_{1p}$  (separation  $d = \sqrt{5}a/2$ ) and  $\phi_{2p}$  ( $d = 3a/2$ ). Trio interactions:  $\phi_{b1t}$  (bent),  $\phi_{b2t}$  (bent), and  $\phi_{tt}$  (triangular). Illustration of conventional and unconventional interactions impacting: (b) periphery diffusion and (c) vacancy-mediated Au diffusion through the interior of a mixed Au–Ag NC. Initial states and transition states (TS) are shown for examples of each type of diffusion process in the same local environments.

the total lateral interaction of the hopping adatom with nearby adatoms in the initial state, the transition state (TS), and the final site, respectively. Then, the  $E_{\text{act}}(\alpha)$  are defined by the exact relation

$$E_{\text{act}}(\alpha) = E_d(\alpha) + \Phi(\text{TS}) - \Phi(\text{init}) \quad (1)$$

Typically,  $\Phi(\text{TS})$  is determined approximately in terms of  $\Phi(\text{init})$  and  $\Phi(\text{fnl})$ . A Metropolis type prescription sets  $\Phi(\text{TS}) = \max[0, \Phi(\text{fnl}) - \Phi(\text{init})] + \Phi(\text{init})$ .<sup>16</sup> An initial value approximation or bond-breaking prescription sets  $\Phi(\text{TS}) = 0$ .<sup>17</sup> A Bronsted–Evans–Polanyi prescription sets  $\Phi(\text{TS}) = c_1\Phi(\text{init}) + c_2\Phi(\text{fnl})$ , usually with  $c_1 = c_2$  for surface diffusion.<sup>18–20</sup> A special choice in this family, and also in the related Butler–Volmer prescription,<sup>21</sup> sets  $c_1 = c_2 = 0.5$ .<sup>22,23</sup> This choice is quite effective for the diffusion subject to weak slowly varying interactions.<sup>23</sup> However, all these choices fail to capture the key features of periphery diffusion even for simple single-component homoepitaxial systems.<sup>11</sup> Various refinements such as the use of distinct Metropolis forms for periphery and intermixing diffusion on the one hand, and for terrace diffusion and attachment-detachment on the other, achieve some improvements for single-component systems<sup>24,25</sup>

but should not be effective for more complex multicomponent systems.

Thus, our approach instead utilizes a multisite lattice-gas (msLG) model formulation, as now described. We restrict attention to a model for 2D Ag–Au NCs on an  $\text{Ag}(100)$  surface, a choice motivated by extensive interest in the formation of 3D core–shell and more complex Ag–Au NCs structures.<sup>1,8,14,15,26</sup> Contrasting previous studies of 3D Ag–Au NCs, we will provide precise atomistic-level modeling of self-assembly on the appropriate time scale and also precisely describe post-assembly sintering. See Figure 1 for a schematic of the model.  $\text{Ag}(100)$  presents a square array of 4-fold hollow (4fh) adsorption sites with surface lattice constant  $a = 0.289$  nm. Surface diffusion is dominated by single-atom hopping between NN 4fh adsorption sites through a well-defined bridge (br) site TS, so the terrace diffusion barriers  $E_d(\alpha)$  for isolated  $\alpha = \text{Ag}$  or Au adatom corresponds to the adsorption energy difference between the br TS and 4fh site. To precisely determine the  $E_{\text{act}}(\alpha)$ , we separately evaluate the components of the “conventional” interactions in  $\Phi(\text{init})$  where all adatoms are at 4fh sites, and the distinct “unconventional” interactions in  $\Phi(\text{TS})$  involving one adatom at a br TS and the others at 4fh

sites. See Figure 1a. It has been recognized that distinct interactions control  $\Phi(\text{TS})$ .<sup>27</sup> However, these have usually been ignored or only roughly estimated, as described above. One more comprehensive study for metal(100) homoepitaxial systems was based on semiempirical potentials,<sup>28</sup> and one study utilized density functional theory (DFT) to assess the interaction of a single nearby adatom on the hopping atom at the TS for Al on Al(110).<sup>29</sup> However, what is needed for predictive KMC simulation of bimetallic NCs is a capability to precisely determine barriers for vast numbers of periphery and bulk configurations,<sup>4,30</sup> a capability provided here.

As an aside, we note that while our model just incorporates single-atom hops, it does capture terrace diffusion of dimers and trimers that occurs by successive single-atom hops (e.g., dimers alternative between configurations with adatoms on NN and second NN sites). The model can be refined to incorporate other concerted processes such as dimer periphery diffusion and exchange of Au with the Ag(100) substrate. However, these processes are not significant for the regime of interest.

All energetics for interactions and barriers are obtained from DFT using the plane-wave VASP code with slab geometries representing the surface, and using the projector augmented wave method.<sup>31,32</sup> The k-point grids are selected to be as close as possible to  $(24 \times 24 \times 1)$  for various primitive surface cells. The energy cutoff for the plane wave basis is 280 eV. Slabs are separated by 1.2 nm of vacuum. Artificial quantum size effects due to electron confinement in thin Ag(100) slabs used in typical DFT calculations are reduced by averaging results over the slabs with thicknesses of 7–12 Ag(100) layers.<sup>33</sup> This averaging is performed for all calculations. Our procedure for DFT analysis is also described elsewhere,<sup>33</sup> and we will comment further below on the dependence of results on the choice of PBE versus PBEsol functional. On the basis of such analysis, below we assign terrace diffusion barriers  $E_d(\text{Ag}) = 0.43$  eV and  $E_d(\text{Au}) = 0.53$  eV. We also estimate a barrier of  $E_{\text{exc}} = 0.69$  eV for Au to exchange with the Ag(100) surface atom. We also note that the initial and final state energies for this exchange are very close, and the exchange pathway used in this analysis is the same as that for exchange diffusion in metal(100) homoepitaxy,<sup>34</sup> a process that dominates over hopping for Pt and Al but not for Ag. As the exchange barrier exceeds the Au diffusion barrier by  $\delta E = 0.16$  eV, this implies an Au diffusion length (before exchange) of  $L_{\text{exc}}(\text{Au}) = ae^{\delta E/(2k_B T)}$ . Unless otherwise stated,  $L_{\text{exc}}(\text{Au})$  is large enough that exchange will not be important for the phenomena analyzed here. Finally, we will adopt prefactors of  $\nu = 10^{12}/\text{s}$  for hopping of aggregated adatoms, and  $10^{13}/\text{s}$  for isolated adatoms, based on previous successful modeling for Ag/Ag(100).<sup>13,35</sup>

One constraint for our general approach is that strain energies be negligible compared with chemical interactions. This applies for Ag–Au epitaxial NC on Ag(100) where there is negligible strain due to the near-perfect match of Au and Ag surface lattice constants. Note that our approach and msLG model also applies directly to analyze other near-strain-free systems, for example, (Pt + Pd)/Pd(100), (Ir + Rh)/Rh(100), and so forth.

**Conventional Adatom Interactions and Thermodynamics.** Previous semiempirical and DFT studies for fcc(100) systems suggest that NN interactions (separation  $d = a$ ) are dominant with second NN ( $d = \sqrt{2}a$ ) and compact trio interactions ~10% of these.<sup>36</sup> We find that this scenario applies for Ag on Ag(100) but not for Au and Au + Ag on Ag(100) where trios are stronger. Thus, we incorporate short-range NN

and second NN pair ( $\omega_{1p}$  and  $\omega_{2p}$ ) and connected linear and bent trio ( $\omega_{lt}$  and  $\omega_{bt}$ ) interactions (see Figure 1a) for all possible combinations of adatoms (see Table 1). Interaction

**Table 1. Values in Electronvolts for Conventional Pair and Trio Interactions Used in our msLG Model (S = Ag and G = Au)<sup>a</sup>**

$\omega_{1p}(\text{SS})$	$\omega_{2p}(\text{SS})$	$\omega_{lt}(\text{SSS})$	$\omega_{bt}(\text{SSS})$
-0.283	-0.027	-0.016	+0.032
$\omega_{1p}(\text{GG})$	$\omega_{2p}(\text{GG})$	$\omega_{lt}(\text{GGG})$	$\omega_{bt}(\text{GGG})$
-0.201	+0.030	-0.065	+0.016
$\omega_{1p}(\text{SG} = \text{GS})$	$\omega_{2p}(\text{SG} = \text{GS})$	$\omega_{lt}(\text{SGG} = \text{GGS})$	$\omega_{bt}(\text{SGG} = \text{GGS})$
-0.285	-0.010	-0.046	+0.026
		$\omega_{lt}(\text{GSS} = \text{SSG})$	$\omega_{bt}(\text{GSS} = \text{SSG})$
		-0.021	+0.036
		$\omega_{lt}(\text{SGS})$	$\omega_{bt}(\text{SGS})$
		-0.022	+0.028
		$\omega_{lt}(\text{GSG})$	$\omega_{bt}(\text{GSG})$
		-0.034	+0.030

<sup>a</sup>The central element listed for trios is in middle. Top row 1: pure Ag. Row 2: pure Au. Rows 3–5: mixed Ag–Au interactions. (Our DFT calculations indicate that interactions obtained from the PBEsol functional are significantly stronger than those from PBE. KMC simulations reveal that the stronger values are needed to recover experimental Ag sintering times. The magnitudes of the listed values are 23% above PBE values.)

values, which include the effect of neglected small longer-range pair and many-body interactions, are obtained from a cluster expansion approach. We expand energies for a large set of  $\sim 30$  pure Ag, pure Au, and mixed adlayer configurations (the latter includes the most favored low-energy configurations) in terms of the retained pair and trio interactions. The latter are then obtained from a least-squares fit to these  $\sim 30$  oversampled DFT energies utilizing a Moore-Penrose pseudoinverse for the relevant linear system. The values obtained from this procedure reported in Table 1 (with S = Ag and G = Au) are used in our KMC simulations.

Next, we explore the consequences of these interactions for adlayer intermixing thermodynamics. The energy per adatom,  $\mu(\alpha)$ , associated with lateral interactions in a complete single-component layer of  $\alpha = \text{Au}$  or Ag yields an effective NN interaction,  $\omega_{\text{eff}}(\alpha\alpha) = \mu(\alpha)/2$ , satisfying

$$\omega_{\text{eff}}(\alpha\alpha) = \omega_{1p}(\alpha\alpha) + \omega_{2p}(\alpha\alpha) + \omega_{lt}(\alpha\alpha\alpha) + 2\omega_{bt}(\alpha\alpha\alpha) \quad (2)$$

so  $\omega_{\text{eff}}(\text{SS}) = -0.262$  eV and  $\omega_{\text{eff}}(\text{GG}) = -0.204$  eV. The energy per adjacent Au–Ag pair,  $\mu(\text{SG})$ , for a perfectly  $c(2 \times 2)$ -ordered Au–Ag overlayer associated with lateral interactions yields an effective NN interaction,  $\omega_{\text{eff}}(\text{SG}) = \mu(\text{SG})/4$ , satisfying

$$\begin{aligned} \omega_{\text{eff}}(\text{SG}) &= \omega_{1p}(\text{SG}) + \frac{1}{2}\omega_{2p}(\text{SS}) + \frac{1}{2}\omega_{2p}(\text{GG}) + \frac{1}{2}\omega_{lt}(\text{SGS}) \\ &\quad + \frac{1}{2}\omega_{lt}(\text{GSG}) + \omega_{bt}(\text{GSG}) + \omega_{bt}(\text{SGS}) \end{aligned} \quad (3)$$

so  $\omega_{\text{eff}}(\text{SG}) = -0.2535$  eV. A preference to produce  $(2 \times 2)$  alloy ordering (relative to Au and Ag phase separation) is indicated by the negative intermixing energy per site,  $\Delta = 2\omega_{\text{eff}}(\text{SG}) - \omega_{\text{eff}}(\text{SS}) - \omega_{\text{eff}}(\text{GG}) = -0.041$  eV. This  $\Delta$  implies an Onsager critical temperature of  $T_c \approx 0.5673|\Delta|/k_B = 270$  K for the  $c(2 \times 2)$  order-disorder transition.

Some features are not captured in the above analysis. For pure NN interactions, bulk  $c(2 \times 2)$  ordering is always preferred for 0.5 monolayers (ML) Au and 0.5 ML Ag when  $\Delta < 0$ . However, enrichment of one species at the periphery of finite NCs is possible, for example, by Au for sufficiently weak  $\omega_{1\text{eff}}(\text{GG})$ , and many-body interactions can induce other types of preferred ordering. However, neither scenario is realized in our system.

Finally, for analysis of core-ring NCs, it will be useful to consider the formation energy for creating an isolated Au (Ag) adatom in a domain of pure Ag (Au) by extracting the adatom from an interface between pure domains. We find that  $E_{\text{form}}(\text{Au in Ag}) = -0.072$  eV versus  $E_{\text{form}}(\text{Ag in Au}) = -0.106$  eV, implying a slight thermodynamic preference for the latter. However, we find that this feature does not control NC composition profiles that are kinetically determined.

**Unconventional (TS) Adatom Interactions and Barriers.** Our model incorporates 30 unconventional interactions for short-range pairs and connected trios (see Figure 1a and Table 2). To reduce the number of independent parameters, we

**Table 2. Values in Electronvolts for Unconventional Pair and Trio Interactions Used in Our msLG Model ( $S = \text{Ag}$  and  $G = \text{Au}$ )<sup>a</sup>**

$\phi_{1\text{p}}(\text{SS})$	$\phi_{\text{b1t}}(\text{SSS})$	$\phi_{\text{b2t}}(\text{SSS})$	$\phi_{\text{tt}}(\text{SSS})$
-0.212	-0.020	-0.003	+0.049
$\phi_{1\text{p}}(\text{GG})$	$\phi_{\text{b1t}}(\text{GGG})$	$\phi_{\text{b2t}}(\text{GGG})$	$\phi_{\text{tt}}(\text{GGG})$
-0.141	-0.031	-0.012	+0.044
$\phi_{1\text{p}}(\text{SG})$	$\phi_{\text{b1t}}(\text{SGG})$	$\phi_{\text{b2t}}(\text{SGG})$	$\phi_{\text{tt}}(\text{SGG})$
-0.188	-0.049	-0.022	+0.059
$\phi_{1\text{p}}(\text{GS})$	$\phi_{\text{b1t}}(\text{GSS})$	$\phi_{\text{b2t}}(\text{GSS})$	$\phi_{\text{tt}}(\text{GSS})$
-0.225	-0.027	-0.007	+0.054
	$\phi_{\text{b1t}}(\text{SGS/SSG})$	$\phi_{\text{b2t}}(\text{SGS/SSG})$	$\phi_{\text{tt}}(\text{SGS} = \text{SSG})$
	-0.038/-0.001	-0.020/+0.007	+0.033
	$\phi_{\text{b1t}}(\text{GSG/GGS})$	$\phi_{\text{b2t}}(\text{GSG/GGS})$	$\phi_{\text{tt}}(\text{GSG} = \text{GGS})$
	-0.011/-0.045	+0.002/-0.023	+0.043

<sup>a</sup>The first element listed is at the br TS for hopping, and the central element of trios is in the middle. Top row 1: pure Ag. Row 2: pure Au. Rows 3–6: mixed Ag–Au interactions. Note that  $\phi_{\text{b2t}}$  values are determined from eq 4, and we also set  $\phi_{2\text{p}} = 0.000, 0.030, 0.020$ , and 0.020 for SS, GG, SG, and GS, respectively.

perform selective large ( $6 \times 6$ ) and ( $10 \times 10$ ) unit cell DFT VASP analysis to assess trends, for example, the strongly bent trio,  $\phi_{\text{b2t}}$ , is well-described by interpolation

$$\phi_{\text{b2t}} \approx \frac{3}{4}\phi_{\text{b1t}} + \frac{1}{4}\phi_{\text{tt}} \quad (4)$$

between the attractive less-bent trio,  $\phi_{\text{b1t}}$ , and the repulsive triangular trio,  $\phi_{\text{tt}}$ . Below, we systematically determine unconventional interactions by demanding that these recover barriers for key periphery or edge diffusion processes.

First, we consider  $\phi$ -interactions associated with edge diffusion for pure Ag and Au NCs. The barrier along close-packed steps,  $E_e(\alpha)$ , and the additional kink or corner rounding barrier,  $E_{\text{kr}}(\alpha)$ , satisfy

$$E_e(\alpha) = E_d(\alpha) + [2\phi_{1\text{p}}(\alpha\alpha) + 2\phi_{\text{b1t}}(\alpha\alpha\alpha) + 2\phi_{\text{b2t}}(\alpha\alpha\alpha) + \phi_{\text{tt}}(\alpha\alpha\alpha)] - [\omega_{1\text{p}}(\alpha\alpha) + 2\omega_{2\text{p}}(\alpha\alpha) + \omega_{\text{lt}}(\alpha\alpha\alpha) + 2\omega_{\text{bt}}(\alpha\alpha\alpha)] \quad (5)$$

and

$$E_{\text{kr}}(\alpha) = -\phi_{1\text{p}}(\alpha\alpha) - \phi_{\text{b1t}}(\alpha\alpha\alpha) - \phi_{\text{b2t}}(\alpha\alpha\alpha) - \phi_{\text{tt}}(\alpha\alpha\alpha) \quad (6)$$

Modified expressions for  $E_e(\alpha)$  apply for  $2 \times 2$  clusters. For pure  $\alpha = \text{Ag}$  (Au) NCs, guided by DFT, we assign  $E_e(\alpha) = 0.30$  (0.38) eV on extended steps,  $E_e(\alpha) = 0.31$  (0.45) eV on  $2 \times 2$  NCs, and  $E_{\text{kr}}(\alpha) = 0.185$  (0.14) eV. The six independent  $\phi$ -values in rows 1 and 2 of Table 2 are selected to recover these six  $E_e$  and  $E_{\text{kr}}$  values.

Second, consider  $\phi$ -interactions associated with edge diffusion for Ag around Au NCs, and of Au around Ag NCs, relevant for description of core-ring NCs. Guided by DFT, we select  $E_e(\alpha) = 0.27$  (0.32) eV on extended steps,  $E_e(\alpha) = 0.33$  (0.36) eV on  $2 \times 2$  NCs, and  $E_{\text{kr}}(\alpha) = 0.20$  (0.205) eV for  $\alpha = \text{Ag}$  (Au) diffusion around Au (Ag) NCs. These energies determine the six independent  $\phi$ -values in rows 3 and 4 of Table 2.

Third, there are six other independent trio  $\phi$ -interactions relevant for diffusion around the periphery of mixed alloy NCs. For a  $2 \times 2$  alloy island starting from a NN site adjacent to the opposite adspecies Ag (Ag), guided by DFT, we select  $E_e(\alpha) = 0.33$  (0.41) eV for edge diffusion and  $E_{\text{kr}}(\alpha) = 0.16$  (0.145) eV for kink rounding for  $\alpha = \text{Ag}$  (Au). A distinct kink rounding barrier,  $E_{\text{kr}}(\alpha) = 0.20$  (0.17) eV for  $\alpha = \text{Ag}$  (Au), applies to round a corner populated by the same adspecies. These energies determine the six additional independent  $\phi$ -values in rows 5 and 6 of Table 2.

**KMC Results for Self-Assembly and Sintering.** First, for model validation we compare predictions with experimental observations for the single-component system Ag/Ag(100). Simulation of Ag NC formation during deposition recovers the observed NC density per adsorption site<sup>11</sup> of  $N \approx 0.23(F/\nu)^{1/3}e^{E_d/(3k_bT)} \sim 4-5 \times 10^{-4}$  at 295 K with  $F = 0.006$  ML/s (recalling that  $E_d = 0.43$  eV). Shapes of isolated Ag NCs, as well as of Ag NC pairs coalescing during growth, are also recovered. See Figure 2. A more demanding test comes from analysis of

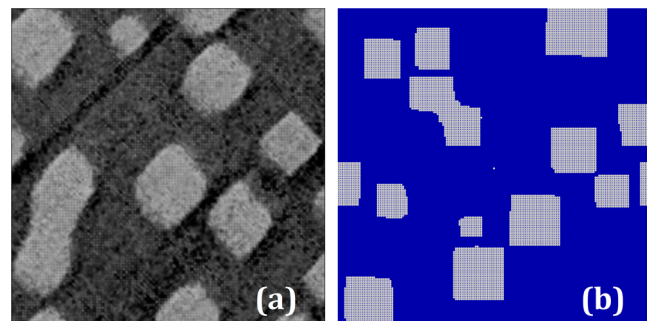


**Figure 2.** (a) STM and (b) KMC images (roughly  $50 \times 50 \text{ nm}^2$ ) of Ag island formation at 295 K with  $F = 0.0022$  ML/s.

post-deposition sintering of two corner-to-corner Ag NCs each with side length  $L \approx 4.8$  nm at 295 K. Simulation predicts a relaxation time of  $\tau = 12-14$  min and also novel size-scaling  $\tau \propto L^3$  (contrasting the prediction  $\tau \propto L^4$  from coarse-grained theory), both consistent with experiment.<sup>13</sup> See Figure 3. Sintering is mediated by periphery diffusion, so that  $\tau \propto e^{-E_{\text{sint}}/(k_bT)}$  with effective barrier  $E_{\text{sint}} = E_{\text{form}}(\text{pd}) + E_{\text{pd}}$ . Here,  $E_{\text{form}}(\text{pd}) = -\omega_{1\text{p}} - \omega_{\text{lt}} - 2\omega_{\text{bt}} = 0.235$  eV for Ag is the formation energy to create an edge adatom from a kink site atom, and  $E_{\text{pd}} = E_e + E_{\text{kr}} = 0.485$  eV for Ag is total periphery diffusion barrier for this atom to round corners or kinks. Thus, we find that  $E_{\text{sint}} = 0.720$  eV is consistent with the above  $\tau$  value

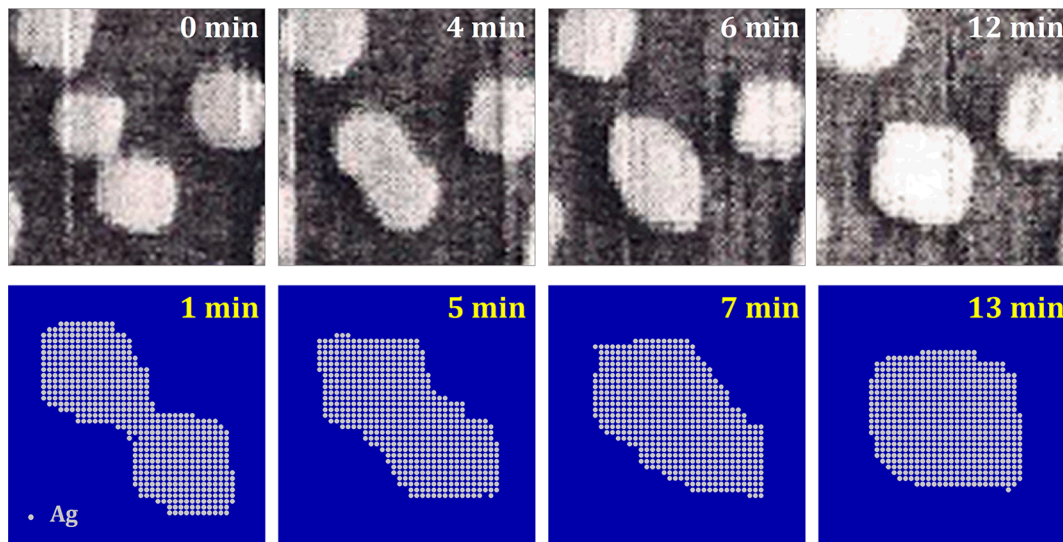


**Figure 3.** Comparison of experimental STM images (upper row) (cf.<sup>13</sup>) and KMC simulation (lower row) for the corner-to-corner sintering of two Ag NCs on Ag(100) at 295 K. Initial cluster sizes are  $5.2 \times 5.2 \text{ nm}^2$  and  $4.8 \times 4.8 \text{ nm}^2$  (STM) and both  $4.9 \times 4.9 \text{ nm}^2$  (KMC).

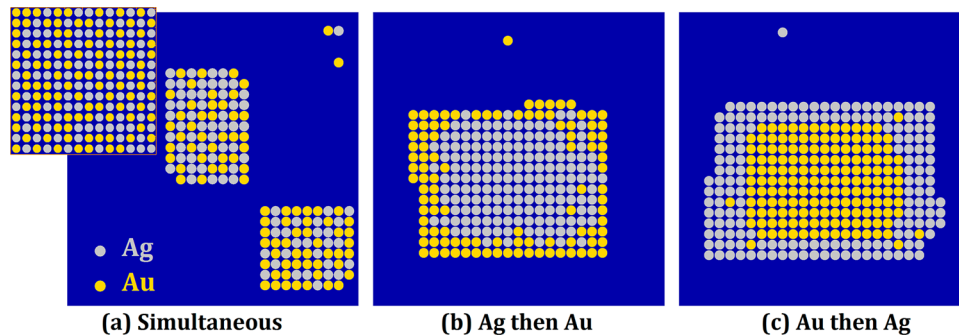


**Figure 4.** KMC simulations of (a) simultaneous deposition; (b) Ag-then-Au, and (c) Au-then-Ag sequential depositions at 295 K with flux  $F = 0.006 \text{ ML/s}$  and roughly equal amounts of Ag and Au. (a) This panel shows  $\sim 80$  Au and  $\sim 80$  Ag, and the inset shows an equilibrated NC structure at 295 K; (b) panel shows  $\sim 160$  Ag and  $\sim 100$  Au; another  $\sim 60$  Au formed two pure Au islands not shown; (c) panel shows  $\sim 160$  Ag and  $\sim 160$  Au.

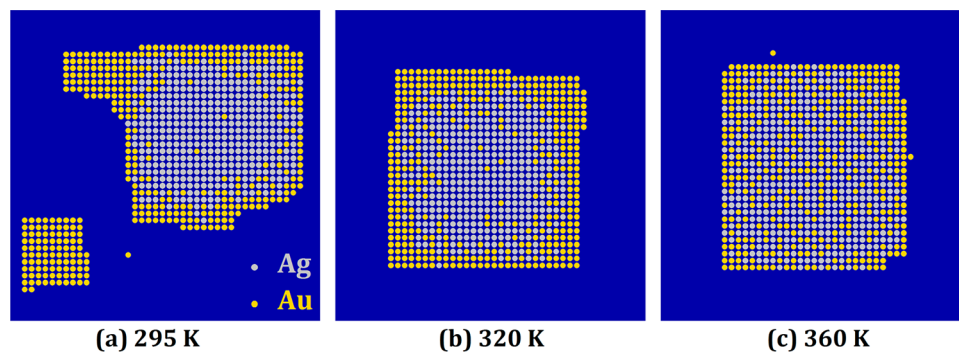


**Figure 5.** KMC simulation assessing the temperature dependence of intermixing for Ag-then-Au deposition. There are  $\sim 400$  Au and  $\sim 400$  Ag atoms in each image.

for Ag.<sup>13</sup> As an aside, simulations for deposition of pure Au on Ag(100) yield a higher Au NC density of  $\sim 20 \times 10^{-4}$  per site at 295 K due to higher  $E_d = 0.53 \text{ eV}$  and slower relaxation times for sintering of Au NC pairs due to higher  $E_{\text{sint}} = 0.754 \text{ eV}$ .

Henceforth, we focus on bimetallic NCs. In Figure 4, we first compare the structure of NCs formed by simultaneous and sequential codeposition at 295 K. Naturally simultaneous codeposition produces mixed NCs, but their structure does not display the degree of  $c(2 \times 2)$  ordering of equilibrated NCs at 295 K. See the inset of Figure 4a. Here, we have efficiently

assessed equilibrium ordering via Metropolis simulation with atom exchange. These Metropolis simulations reveal the expected long-range  $c(2 \times 2)$  order below  $\sim 270$  K. We also note that simultaneous codeposition at 295 K yields a density of around  $\sim 15 \times 10^{-4}$  per site for mixed NCs that is between that for pure Ag and pure Au NCs. This is qualitatively (but not quantitatively) consistent with the prediction of mean-field theory.<sup>37</sup> In contrast, sequential codeposition at 295 K produces core-shell NC with limited intermixing at the interface between the Ag- and Au-rich regions. However, there is some

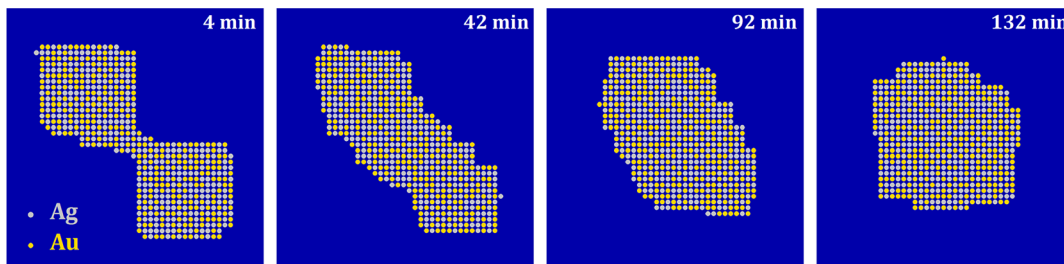


**Figure 6.** KMC simulation results for the sintering of two  $4.9 \times 4.9 \text{ nm}^2$  Ag–Au mixed NCs at 295 K.

indication of an asymmetry between the population of Au in Ag regions and vice versa. Here it should be mentioned that in the simulation of Figure 4c we first deposited Au at 330 K to create larger Au islands before  $T$  was lowered to 295 K for subsequent Ag deposition.

For a more comprehensive assessment of intermixing, we consider  $T$ -dependence for sequential deposition of Ag followed by Au (considering larger islands than above). Au atoms deposited away from far-separated Ag islands at higher  $T$  will exchange with the substrate and/or nucleate pure Au NCs, but those deposited within a distance  $L_{\text{exc}}(\text{Au})$  of the edge of Ag NCs will aggregate with those NCs forming an Au ring. Results reveal a strong increase in the degree of intermixing increasing  $T$  from 295 to 320 to 360 K. See Figure 5. The asymmetry revealed in a high Au population of Ag regions, but not the reverse, is also more dramatic at higher  $T$ .

Next, for core–ring NCs we provide a detailed atomistic-level characterization of intermixing dynamics that is mediated by the diffusion of vacancies through the NC. These vacancies allow shuffling of Au and Ag positions in the absence of place-exchange, which is prohibitive for this system. The above-mentioned asymmetry might be associated with a Kirkendall effect for diffusion couples. This view would suggest that diffusion of Au into Ag regions is more facile than the opposite, a feature that would induce a net vacancy diffusion flux in the direction of the faster diffusing Au (and which could lead to void formation in certain conditions). Beyond speculation, we can utilize our msLG model to directly determine the effective barriers for Au diffusion through Ag regions, and Ag diffusion through Au regions. We first note that the effective barrier  $E_d(\text{Au in Ag})$  for diffusion of Au through Ag regions is given by

$$E_d(\text{Au in Ag}) = E_{dv}(\text{Au in Ag}) + E_{\text{form}}(\text{v-Au in Ag}) \quad (7)$$

where  $E_{dv}(\text{Au in Ag}) = 0.350 \text{ eV}$  is the vacancy diffusion barrier to exchange a diffusing Au atom and adjacent vacancy (v) within Ag, and  $E_{\text{form}}(\text{v-Au in Ag}) = 0.441 \text{ eV}$  is the formation energy to create a vacancy next to Au (where the vacancy comes from the NC periphery). Thus, we have  $E_d(\text{Au in Ag}) = 0.791 \text{ eV}$ .

Similarly for diffusion of Ag through Au, we find that  $E_{dv}(\text{Au in Ag}) = 0.403 \text{ eV}$  and  $E_{\text{form}}(\text{v-Ag in Au}) = 0.460 \text{ eV}$ , so that  $E_d(\text{Au in Ag}) = 0.863 \text{ eV}$ . The lower  $E_d(\text{Au in Ag})$  value results in significant diffusivity for Au through Ag regions (in contrast to Ag through Au) for the temperature range of interest. Thus, we conclude that the dominance of isolated Au in Ag regions versus the opposite is kinetic in origin, overwhelming the above-mentioned thermodynamic preference for Ag in Au regions.

Finally, we consider the post-assembly sintering of a pair of alloy NCs at 295 K. The initial structure of the individual NCs is equilibrated from the Metropolis approach with atom

exchange. Simulation results presented in Figure 6 show that sintering is much slower compared to pure Ag NCs of the same size (cf. Figure 3). This behavior can be understood by utilizing our msLG model to assess relevant sintering barriers. Many local NC structures are possible, but it should suffice to assess behavior for the predominant  $c(2 \times 2)$  alloy ordering. The energy to form an Ag edge adatom on the most favored edge site starting from a kink site is  $E_{\text{form}}(\text{pd}) = 0.249 \text{ eV}$ , the edge diffusion barrier is  $E_e = 0.316 \text{ eV}$ , and the highest extra barrier for rounding kinks is  $E_{kr} = 0.213 \text{ eV}$ , so summing gives  $E_{\text{sint}} = 0.778 \text{ eV}$ . Similarly, the formation energy for Au edge atoms is  $E_{\text{form}}(\text{pd}) = 0.245 \text{ eV}$ , the edge barrier is  $E_e = 0.345 \text{ eV}$ , and the highest extra barrier for rounding kinks is  $E_{kr} = 0.191 \text{ eV}$ , so  $E_{\text{sint}} = 0.781 \text{ eV}$ . These higher  $E_{\text{sint}}$  values (cf. 0.720 eV for pure Ag NCs) explain the 10-fold increase in relaxation time at 295 K.

In summary, we provide a framework for ab initio atomistic-level description of the critical kinetics of periphery diffusion and intermixing processes in bimetallic NCs. This is based on an algorithm to precisely determine the vast number of distinct barriers for these processes for different local environments and enables realistic and predictive simulation on the appropriate time scale of self-assembly and sintering processes.

## ■ AUTHOR INFORMATION

### Corresponding Author

\*E-mail: yhan.ameslab@gmail.com; yong@ameslab.gov.

### Notes

The authors declare no competing financial interest.

## ■ ACKNOWLEDGMENTS

We thank Conrad Stoldt and Patricia Thiel for access to sintering data for Ag NCs supplementing that published previously. We also thank Vladimir Zhdanov for useful discussions. Y.H. and J.E. were supported for the kinetic modeling by NSF Grant CHE-1111500. D.J.L. was supported for the DFT analysis by the USDOE BES Division of Chemical Sciences, Geosciences, and Biosciences through the Chemical Physics project at Ames Laboratory, which is operated by Iowa State University under Contract No. DE-AC02-07CH11358. Computations utilized USDOE NERSC and NSF-supported XSEDE resources.

## ■ REFERENCES

- (1) Xia, Y.; Xia, X.; Wang, Y.; Xie, S. *MRS Bull.* **2013**, *38*, 335–343.
- (2) Xia, X.; Xie, S.; Liu, M.; Peng, H.-C.; Lu, N.; Wang, J.; Kim, M. J.; Xia, Y. *Proc. Natl. Acad. Sci. U.S.A.* **2013**, *110*, 6669–6673.
- (3) Liu, X.; Wang, D.; Li, Y. *Nano Today* **2012**, *7*, 448–466.
- (4) Duguet, T.; Han, Y.; Yuen, C.; Jing, D.; Unal, B.; Evans, J. W.; Thiel, P. A. *Proc. Natl. Acad. Sci. U.S.A.* **2011**, *108*, 989–994.

- (5) Brune, H. In *Handbook of Surface Science*; Hasselbrink, E., Lundqvist, B. I., Eds.; Elsevier: Amsterdam, 2008; Vol. 3, Chapter 15.
- (6) Bartelt, M. C.; Schmid, A. K.; Evans, J. W.; Hwang, R. Q. *Phys. Rev. Lett.* **1998**, *81*, 1901–1904.
- (7) Marsault, M.; Hamm, G.; Wörz, A.; Sitja, G.; Barth, C.; Henry, C. R. *Faraday Discuss.* **2008**, *138*, 407–420.
- (8) Benten, W.; Nilius, N.; Ernst, N.; Freund, H.-J. *Phys. Rev. B* **2005**, *72*, 045403.
- (9) Whitesides, G. M.; Grzybowski, B. *Science* **2002**, *295*, 2418–2421.
- (10) Michely, T.; Krug, J. *Islands, Mounds, and Atoms*; Springer: Berlin, 2004.
- (11) Evans, J. W.; Thiel, P. A.; Bartelt, M. C. *Surf. Sci. Rep.* **2006**, *61*, 1–128.
- (12) Seyed-Razavi, A.; Snook, I. K.; Barnard, A. S. *Cryst. Growth Des.* **2011**, *11*, 158–165.
- (13) Stoldt, C. R.; Cadilhe, A. M.; Jenks, C. J.; Wen, J.-M.; Evans, J. W.; Thiel, P. A. *Phys. Rev. Lett.* **1998**, *81*, 2950–2953.
- (14) Gonzalez, E.; Arbiol, J.; Puntes, V. F. *Science* **2011**, *334*, 1377–1380.
- (15) Yin, Y.; Erdonmez, C.; Aloni, S.; Alivisatos, A. P. *J. Am. Chem. Soc.* **2006**, *128*, 12671–12673.
- (16) Landau, D. P.; Binder, K. *A Guide to Monte Carlo Simulations in Statistical Physics*; Cambridge UP: Cambridge, 2000.
- (17) Ala-Nissila, T.; Ferrando, R.; Ying, S. C. *Adv. Phys.* **2002**, *51*, 949–1078.
- (18) Bronsted, J. N. *Chem. Rev.* **1928**, *5*, 231–338.
- (19) Evans, M. G.; Polanyi, M. *Trans. Faraday Soc.* **1938**, *34*, 11–24.
- (20) Liu, D.-J.; Evans, J. W. *Prog. Surf. Sci.* **2013**, *88*, 393–521.
- (21) Smickler, W. *Interfacial Electrochemistry*; Oxford University Press: Oxford, 1996.
- (22) Brown, G.; Rikvold, P. A.; Mitchell, S. J.; Novotny, M. A. In *Interfacial Electrochemistry: Theory, Experiment, and Application*; Wieckowski, A., Ed.; Marcel Dekker: New York, 1999; p 47–61.
- (23) Fichthorn, K. A.; Scheffler, M. *Phys. Rev. Lett.* **2000**, *84*, 5371–5374.
- (24) Heinonen, J.; Koponen, I.; Merikoski, J.; Ala-Nissila, T. *Phys. Rev. Lett.* **1999**, *82*, 2733–2736.
- (25) Han, Y.; Liu, D.-J.; Unal, B.; Qin, F.; Jing, D.; Jenks, C. J.; Thiel, P. A.; Evans, J. W. *Phys. Rev. Lett.* **2008**, *100*, 116105.
- (26) Shore, M. S.; Wang, J.; Johnston-Peck, A. C.; Oldenburg, A. L.; Tracy, J. B. *Small* **2011**, *7*, 230–234.
- (27) Zhdanov, V. P. *Elementary physicochemical processes on solid surfaces*; Plenum: New York, 1991.
- (28) Mehl, H.; Biham, O.; Furman, I.; Karimi, M. *Phys. Rev. B* **1999**, *60*, 2106–2116.
- (29) Tiwary, Y.; Fichthorn, K. A. *Phys. Rev. B* **2010**, *81*, 195421.
- (30) Han, Y.; Unal, B.; Evans, J. W. *Phys. Rev. Lett.* **2012**, *108*, 216102.
- (31) Kresse, G.; Furthmuller, J. *Comput. Mater. Sci.* **1996**, *6*, 15–50.
- (32) Bloechl, P. E. *Phys. Rev. B* **1994**, *50*, 17953–17979.
- (33) Liu, D.-J. *Phys. Rev. B* **2010**, *81*, 035415.
- (34) Kellogg, G. L.; Feibelman, P. J. *Phys. Rev. Lett.* **1990**, *64*, 3143–3146.
- (35) Caspersen, K. J.; Layson, A. R.; Soldt, C. R.; Fourneau, V.; Thiel, P. A.; Evans, J. W. *Phys. Rev. B* **2002**, *65*, 193407.
- (36) Stasevich, T. J.; Einstein, T. L.; Stolbov, S. *Phys. Rev. B* **2006**, *73*, 115426.
- (37) Einax, M.; Ziehm, S.; Dieterich, W.; Maass, P. *Phys. Rev. Lett.* **2007**, *99*, 016106.